The Planetary Science Journal, 3:139 (13pp), 2022 June https://doi.org/10.3847/PSJ/ac67de

The Influence of Surface Binding Energy on Sputtering in Models of the Sodium Exosphere of Mercury

Rosemary M. Killen[1], Liam S. Morrissey[2], Matthew H. Burger[3], Ronald J. Vervack, Jr.[4], Orenthal J. Tucker[1], and Daniel W. Savin[5]
[1] NASA Goddard Space Flight Center, Planetary Magnetospheres Laboratory, Code 695, Greenbelt, MD 20771, USA; rosemary.killen@nasa.gov
[2] NASA Goddard Space Flight Center/Catholic University, Washington, DC 20005, USA
[3] Space Telescope Science Institute, 3700 San Martin Drive, Baltimore, MD 21218, USA
[4] Johns Hopkins Applied Physics Laboratory, 11100 Johns Hopkins Road, Laurel, MD 20723, USA
[5] Columbia Astrophysics Laboratory, Columbia University, MC 5247, 550 West 120th Street, New York, NY 10027, USA
Received 2021 December 2; revised 2022 March 29; accepted 2022 April 15; published 2022 June 14

Abstract

We have simulated the sodium (Na) exosphere of Mercury to show how the exosphere is affected by the assumed surface binding energy (SBE) of Na in the sputtered component. We constrained ion precipitation onto the surface using distributions for the cusp regions that are consistent with measurements by the MErcury Surface, Space ENvironment, GEochemistry, and Ranging Fast Imaging Plasma Spectrometer instrument. We have simulated sputtering with SBEs of 0.27, 2.6, 4.4, and 7.9 eV, with the lowest value commonly used in exosphere models and the highest from recent molecular dynamics calculations for the Na-bearing feldspar end-member, albite. A gradual change in the exosphere is seen as the yield decreases and the ejecta energy increases with increasing SBE. We describe the corresponding exosphere source functions for ion sputtering (IS), as well as for the previously studied processes of micrometeoroid impact vaporization and photon-stimulated desorption (PSD), along with their release energy distributions and spatial distributions. We have summed the contributions of the various source processes to explain how and when the different sources can be distinguished by observations. The modeled exosphere scale heights range from 72 km for PSD to over 1000 km for IS using a SBE of 7.9 eV. We find that the processes responsible for generating Mercury's Na exosphere are separable by measuring line-of-sight column densities tangent to the planet at various altitudes and positions around the planet. Our initial results are consistent with the Na being sputtered from a high-SBE material such as feldspar, which has been predicted to be abundant on the Mercury's surface.

Unified Astronomy Thesaurus concepts: Mercury (planet) (1024); Exosphere (499)

1. Introduction

Mercury possesses what is known as a surface-bounded exosphere, in which particles are not expected to interact with other exospheric particles (Killen & Ip 1999; Stern 1999; Killen et al. 2007). Because the exosphere is collisionless, different species or different sources of a single species can be modeled separately using Monte Carlo techniques without having to incorporate interactions. This makes Monte Carlo modeling a particularly useful tool for deciphering the important physical processes at play in the creation and maintenance of the Hermean exosphere. These processes included ion sputtering (IS), photon-stimulated desorption (PSD), and micrometeoroid impact vaporization (IV). When modeling ion sputtering from mineral surfaces, a key input parameter is the surface binding energy (SBE) of the atom being considered. Our main goal here is to show the effects of the Na SBE on the sputtered component of the Na exosphere and that the relative contributions of IS, PSD, and IV can be inferred from targeted observations of the exosphere.

The Na SBEs used in previous models of the Hermean exosphere have varied by nearly an order of magnitude, from 0.27 eV (Wiens et al. 1997; Leblanc & Johnson 2003) to 2.65 eV (Lammer et al. 2003). The work of Morrissey et al. (2022) demonstrated that the SBE of Na in minerals expected to occur on the surface of Mercury can be as high as or higher than 7.9 eV. Because the sputtering yield and energy distribution are highly dependent on the Na SBE, which varies with the surface mineral and the state of the surface, which can be altered through space weather (i.e., amorphization, etc.), it is important to understand the implications of these values for the exosphere. As such, we have compared Na exospheres simulated using the yield and velocity distribution described as a function of Na SBE from Morrissey et al. (2022) assuming 1 keV solar wind protons impacting onto albite at normal incidence to compare with available exosphere observations. To present a complete picture of the exosphere we include source processes previously considered in models: PDS, IV, and IS.

2. Hermean Exosphere Model

We utilize a Monte Carlo model developed for the sourcing, migration, and loss of particles in a surface-bounded exosphere such as Mercury's (Burger et al. 2010, 2012, 2014). This model is similar to those developed by others (e.g., Hodges 1973; Arnold 1979; Butler 1997; Crider & Vondrak 2000; Wurz & Lammer 2003). More specifically, we use the model of Burger et al. (2012, 2014), rewritten to be compatible with Python 3.6 or above and archived on github. The update to Python has resulted in considerable reduction in

Table 1
Miscellaneous Parameters

PSD	Minimum $Q = 1 \times 10^{-20}$, Maximum $Q = 3 \times 10^{-20}$, T = 1200 K
IV	Min. Rate = 1×10^5 cm^{-2} s^{-1}, Max. Rate = 2.1×10^6 cm^{-2} s^{-1} at 0.352 au
Sticking	Temperature dependent
Accommodation	0.5

run time, making it ideal for carrying out a multitude of simulations in a short time.

The model follows the paths of packets representing collections of particles under the effects of gravity and radiation pressure after the particles have been released into the exosphere. Initial energies are obtained from a distribution function for the selected source process. The number of particles the packet represents is reduced by photoionization, photodissociation (for molecular species), gravitational escape, and/or collisions with the surface. When a surface collision occurs, a specified fraction of the packet sticks to the surface (i.e., the number of particles the packet represents is reduced); the remainder may bounce for another ballistic hop, accommodate to the surface temperature (i.e., thermalize), or exchange energy with the surface and be released with a new energy. Complete sticking, temperature-dependent sticking, no sticking, or a sticking coefficient from a surface map are all user-specified options. The user can additionally specify whether the atom will accommodate to the surface temperature, partially accommodate, or elastically scatter. Packets that escape beyond the Hill sphere are considered to have gravitationally escaped. At some point, the particles will either be lost from the exosphere or will arrive in a cold trap. The Monte Carlo model records particle positions and velocities at user-defined times, fluxes to specific points on the surface, and loss rates. The model does not currently keep track of atoms that stick on the surface, but only records that they are lost from the exosphere. Most components of the model are modular such that various sources, losses, and physics can be selected by the user to explore the effects these have on the atmosphere.

Through various assumptions in the modeling, one can create a set of "base exospheres" that will have a characteristic distribution of particles for the assumed initial distribution and physics involved. Different base exospheres can be combined in proportion to their source rates to produce an aggregate exosphere. Variations and combinations can then be employed to explore the important physical mechanisms thought to be dominant, and model results can easily be compared to observational data. Finding the combination that best matches the data—instantaneously, on average, or in response to drivers—reveals what sources, sinks, or physical processes are important in controlling the exospheric distribution. This motivates the simulations of the Hermean exosphere described here, where the focus of this paper is to explain the implications of the assumed SBE of the Na in the Hermean regolith on the sputtering yield and distribution, and to determine where and when any sputtering-derived exosphere can be extracted from observations of the full Na exosphere. A follow-on paper will utilize these base models for comparisons to data from the MErcury Surface, Space ENvironment, GEochemistry, and Ranging (MESSENGER; Solomon et al. 2007) mission to determine where they match and where they fail, thus constraining the exospheric processes.

2.1. Ballistic Motion

After release from the surface at a given position, with a velocity vector selected from an appropriate distribution function, the model calculates the particle's trajectory under gravity and radiation pressure using a fifth-order Runge–Kutta (RK5) algorithm (Press et al. 2007). Migrating particles follow a ballistic trajectory once released from the surface because the exosphere is collisionless. Our model includes radiation pressure as described in Burger et al. (2010). The acceleration due to radiation pressure, a_r, on a Na atom is given by

$$a_r = \Sigma h g_i/(m(\mathrm{Na})\,\lambda_\iota), \quad (1)$$

where h is Planck's constant, λ_i are wavelengths of the resonant transitions, g_i are the g values of each transition (a solar-forced g value defined as an emission probability per atom (photons s^{-1} atom^{-1})), and m(Na) is the mass of the Na atom. Thus, the magnitude of the radiation pressure and the resonant-scattering rate both depend on the g values, appropriately calculated for the Doppler shift as a function of the instantaneous heliocentric velocity of each atom. The radiation pressure is calculated at each time step. The summation is taken over the relevant transitions.

2.2. Source Functions

The Monte Carlo model, previously used to model Mercury's exosphere (Burger et al. 2010, 2012, 2014), takes a source function appropriate for each source process we intend to simulate (including spatial and energy distributions) and calculates the trajectories of large numbers of packets representing bundles of atoms. A separate exosphere model is run for each source process. The number of atoms simulated is large enough to provide reasonable statistics but not an unduly long run time, with each resulting run subsequently scaled to the total assumed source rate for the given model source process. The exospheres for each process are then added. For comparisons to MESSENGER Mercury Atmospheric and Surface Composition Spectrometer (MASCS) data (Section 5), the scaling can be adjusted to fit the data. The code is able to incorporate the different source functions required for each process at work on Mercury, including PSD, thermal desorption (TD), IS, IV, outgassing, and large impact events (e.g., Killen & Ip 1999). The PSD rate is given by Equation (1), the IV rate is given by either the minimum or maximum rate (Table 1) with the Na flux distributed according to a source function having a Gaussian distribution centered on the dawn equator (Section 2.2.2, the same general distribution used by Burger et al. 2012, 2014 to fit MESSENGER MASCS observations of calcium). The sputter contribution is distributed and scaled as described in Section 2.2.3.

The primary sources as defined in this paper are those that release atoms from the rocky surface and provide atoms that subsequently either escape or adsorb onto the surface. These particles are tracked by the code and continue to be reejected

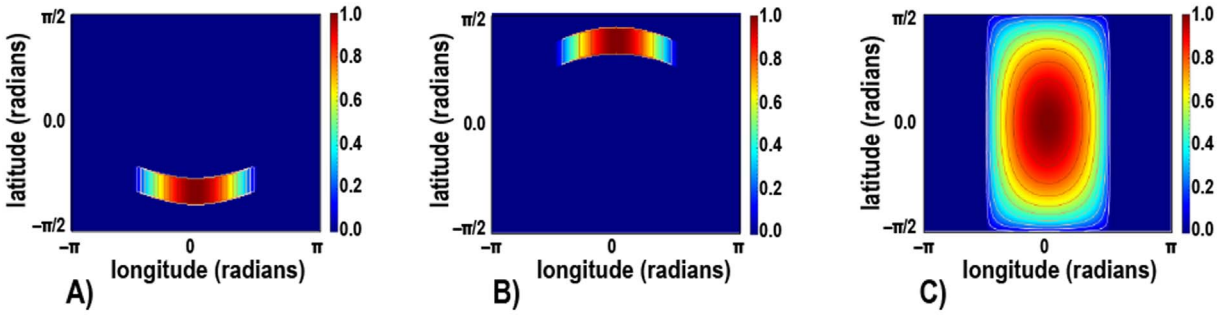

Figure 1. (a)–(b) Surface maps for IS in the south and north, respectively. The IS surface maps are based on measurements of the northern cusp by the MESSENGER FIPS instrument (Raines et al. 2014). They are only used as a reasonable basis for illustrating the differences resulting from the different SBE values, and are not necessarily reflective of actual open cusp areas at Mercury, especially in the southern hemisphere where similar measurements are not available. (c) Source map for PSD. The scaling is informed by fits to the MESSENGER MASCS data and diffusion-limited supply (Burger et al. 2010).

with no, partial, or full thermal accommodation until they are removed by photoionization, gravitational escape, or sticking to the surface. Outgassing is normally only considered for noble gases such as Ar and Ne. We do not consider large impact events because they are random events for which the effects are not long lasting (Mangano et al. 2007). TD is not considered as a separate source process because it is not a primary source process in the sense that the atoms which thermally desorb are not ejected from the mineral rock per se. Recent work shows that high surface activation energy expected on space-weathered surfaces reduces or precludes TD, and that, in addition, TD is very low for atomic species having less than a monolayer coverage (Farrell et al. 2015a, 2015b, 2016). In our model, when an atom encounters the surface it will either stick or become reemitted depending on the input parameters used for the particular simulation. If surface accommodation is specified, the atom will be reemitted as a thermal atom. In this way TD is implicitly included.

An input flux and spatial distribution are assigned as appropriate for each source: solar ultraviolet (UV) radiation for PSD (Section 2.2.1), micrometeoroid flux for IV (Section 2.2.2), and solar particle flux into the cusp region for IS (Section 2.2.3). Particles ejected by a given release process are taken from a user-specified source map that defines the relative source strength and area from which ejected atoms are released. For instance, depending on the process, the source map may represent variations in the surface composition, describe spatial variations in the flux of incoming UV for PSD, track the expected influx of ions (e.g., Fatemi et al. 2020) for IS source maps, or map the expected spatial distribution of micrometeoroid flux for IV. We use an analytical function for the distribution of IV ejecta based on the distribution determined for Ca by Burger et al. (2012, 2014) instead of a surface map. Source maps are user-supplied for each run, and the source map pixels are scaled from 0 to 1 (i.e., a relative scale). A pixel with source map value 1 will be assigned the maximum source rate for that process. The source rate is scaled to the fraction of the maximum source rate as assigned by the value of the pixel. Source maps for IS and PSD are shown in Figure 1. We assign the ejected products an initial velocity from the surface drawn from the distribution function appropriate to the release mechanism (Roth 1983; Hofer 1991; Burger et al. 2010, 2012, 2014).

In order to correlate the source rate with an exospheric distribution, a start time is assigned to the particles in the simulation at random within a specified time window. That way, each particle is weighted by the ratio of the number of simulated particles per length of the time window to the number of particles released per second by the given source.

2.2.1. Photon-stimulated Desorption (PSD)

PSD was first suggested as a source for Mercury's Na exosphere by McGrath et al. (1986). Subsequent laboratory studies of PSD from surfaces that simulate lunar silicates used UV photons with wavelengths <300 nm and established an absorption cross section of $Q = (3 \pm 1) \times 10^{-20}$ cm^2 at 5 eV (Yakshinskiy & Madey 1999). The solar photon flux at $h\nu >$ 5 eV (above the bandgap energy) is $F_{\rm ph} = 10^{14}$ photons cm^{-2} s^{-1}, where h is Planck's constant and ν is the frequency of the photon. The PSD-generated Na flux, $\Phi^{\rm PSD}$, is calculated using $F_{\rm ph}$, scaled by a surface map that takes into account the curvature of the planet and space-weathering considerations (such as ion-enhanced diffusion or deep dielectric discharge in cold regolith that can change with latitude and longitude), and is given by the source function

$$\Phi^{\rm PSD} = F_{\rm ph} Q \sigma / R_h^2, \quad (2)$$

where σ is the Na surface coverage, taken to be the fractional Na abundance, $f_{\rm Na,}$ times the surface number density, $n_{\rm s}$, and R_h is Mercury's orbital distance from the Sun (heliocentric distance). The fraction of Na by number, $f_{\rm Na}$, is assumed to be between 2% (equatorial) and 5% (north volcanic plains) based on MESSENGER observations (Peplowski et al. 2014). The surface number density, $n_{\rm s} = 7.4 \times 10^{14}$ cm^{-2}, is derived from

$$n_{\rm s} = \left(\frac{\rho N_{\rm A}}{\overline{m}} \right)^{2/3}, \quad (3)$$

assuming a mass density in the regolith of $\rho = 0.811$ g cm^{-3} (Ohtake et al. 2010) and an average atomic mass unit (amu) of $m \approx 24$ amu determined from the stoichiometry from the composition of Nittler et al. (2011); $N_{\rm A}$ is Avogadro's number. Note that $n_{\rm s}$ is not the density of the mineral grains that make up the regolith.

Cassidy & Johnson (2005) reduced the PSD cross section by a factor of three to account for trapping of the ejected atoms in the regolith. Sarantos & Tsavachidis (2020) considered diffusion into the regolith as an efficient sink for exospheric atoms. In our models we considered PSD yields beginning with the Yakshinskiy & Madey (1999) yield reduced by a factor of three as suggested by Cassidy & Johnson (2005), $Q = 1 \times 10^{-20}$ cm^2, and subsequently considered the yield

based on the measured PSD cross section, $Q = 3 \times 10^{-20}$ cm^2. We use a thermal velocity distribution with a temperature of 1200 K (Madey et al. 1998; Yakshinskiy & Madey 1999, 2003). We use a PSD source function that falls off as $\cos^{1/2}(\mu)$ $\cos^{1/2}(\lambda)$, where μ is latitude and λ is longitude, measured from the subsolar point. Although the fluxes of the solar photons fall off as $\cos(\psi)$, the total spherical angle from the subsolar point, dielectric breakdown, which is predicted to deposit an energy flux that increases from the equator to the poles (Jordan et al. 2019), should cause the latitudinal profile of net PSD to be flatter than if just solar flux dominated. Burger et al. (2010) found that the PSD flux was limited across most of the dayside by the diffusion rate of Na to the surfaces of grains, and that this rate was enhanced by ion precipitation. Observations of the lunar exosphere inside the Earth's magnetosphere (Potter et al. 2000) support feedback between ion impact and PSD (Sarantos et al. 2008), which would flatten the PSD source function. Along the equator, where $\cos(\mu) = 1$, the PSD source falls off from the subsolar point as $\cos^{1/2}(\lambda)$.

2.2.2. Impact Vaporization (IV)

IV due to micrometeoroid impact was considered as a possible source of the Na and K exospheres of Mercury by Morgan et al. (1988). The importance of IV was shown by Hunten et al. (1998), who observed a brightening of the lunar Na tail after the passage of the Moon through the Leonid meteor stream. Impact-induced exospheres produced by micrometeoroids of mass <0.1 g were modeled for both Mercury and the Moon by Cintala (1992). Meteoroids of mass >0.1 g were considered as sources of a transient exosphere (Mangano et al. 2007), and short-lived effects possibly due to such "larger" impacts are reported to have been seen by MESSENGER (Cassidy et al. 2021). Our goal is to compare the sputter component of the exosphere with the other regular exospheric sources, thus we have used upper and lower limits on IV derived from ground-based and MESSENGER observations made on 2008 January 14, and modeled by Mouawad et al. (2011). Further details on micrometeoroids as sources for exospheres can be found in Janches et al. (2021).

The IV-generated Na flux, Φ^{IV}, found by Mouawad et al. (2011) depended on the modeled fluxes and parameters for the other processes, and was given limits based on possible fits to all available data such that $1 \times 10^5 < \Phi^{IV} < 2 \times 10^6$ cm^{-2} s^{-1}. We modeled IV with a Gaussian spot centered at the dawn terminator on the equator with an e-folding width, σ_g, of 50° as found by Burger et al. (2012, 2014) for Ca at Mercury. The value of Φ^{IV} given above is that at the maximum of the Gaussian distribution. This is consistent both with Ca, assumed to be ejected solely by IV, and with the findings of the Lunar Atmosphere and Dust Environment Explorer, which showed impacts at the Moon centered on the dawn hemisphere in the ram direction of the lunar motion (Horanyi et al. 2015). The area in the IV region, calculated on a spherical surface and scaled to the Gaussian function, is 7.98×10^{16} cm^2. The impact-generated sodium flux was rescaled for this work from that appropriate at 0.352 au during the Mouawad et al. (2011) observations to heliocentric radial distances corresponding to the true anomaly angle (TAA) of 26° (0.313 au) or 144° (0.444 au) as appropriate for the simulation.

2.2.3. Ion Sputtering (IS)

Sputtering of Na by solar wind ions impinging onto the surface of Mercury through the cusps of the magnetosphere was first suggested by Potter & Morgan (1990) to explain rapid variations in the observed Na exosphere, with high- to mid-latitude enhancements appearing and disappearing on intervals less than a day. Such variations cannot be attributed to PSD, which varies slowly with the TAA of the planet and is also characterized by a subsolar (or near-subsolar) maximum in the distribution. Variations in the Na exosphere during a week-long sequence in 1997 November were shown to correlate with possible variations in Mercury's magnetosphere, such that increased IS correlated with opening of the cusp regions and an increased ion flux to the surface (Killen et al. 2001; Sarantos et al. 2007).

At Mercury, the solar wind generally impacts the dayside surface along open field lines, or near the open–closed boundary region (Kallio & Janhunen 2003a, 2003b; Sarantos et al. 2007; Raines et al. 2014). Plasma from Mercury's magnetosphere will impinge on the nightside of Mercury, generally at lower latitudes and at much lower fluxes than the dayside cusp regions (Korth et al. 2014; Fatemi et al. 2020). We have not simulated nightside sputtering because our focus is on observations of the dayside of the planet. At times, possibly when a coronal mass ejection (CME) or solar energetic particle event reaches Mercury, the solar wind can potentially impact the entire sunward side (Kabin et al. 2000; Kallio & Janhunen 2003a), as reported to have been observed by Slavin et al. (2019) and modeled by Jia et al. (2019) and Fatemi et al. (2020).

Sputtering by H^+, which on average accounts for 85% of the total kinetic energy carried by the ~1 keV amu^{-1} solar wind, is relatively inefficient. In contrast, He^{2+} accounts for about 14% of the kinetic energy carried by the solar wind, but has a significantly higher sputtering yield than H^+ (e.g., Eckstein 2007). The composition of the solar wind is variable (Von Steiger et al. 2000), but H^+ and He^{2+} account for much of the space-weathering effects observed on the Hermean surface (Mutzke et al. 2019). The sputtering yield of heavier ions is high, but the fraction of heavy ions is low in the solar wind (i.e., ions with atomic numbers, Z, beyond that for He). However, the fraction of heavy ions in the solar wind increases dramatically in a CME or solar magnetic cloud.

Although heavy ions ($Z > 6$) account for only about 2% of the kinetic energy carried by the solar wind, they carry potential energy owing to their ionization, on the order of 1 keV per ion (Krachner et al. 2003). The charge state of the impinging ion has little effect on the sputter efficiency of highly conducting targets (conductors and semiconductors), but it may have a considerable effect on insulators (Aumayr & Winter 2004). Sputtering of surfaces by highly charged projectiles, in which the potential energy of ionization contributes significantly to the yield, is called potential sputtering. We have not considered potential sputtering by heavy highly charged ions, but based on the results of Killen et al. (2012) and Hijazi et al. (2014, 2017), we expect that potential sputtering could increase the importance of IS by less than a factor of two.

2.3. Loss Processes

Atoms may be ejected into the exosphere above escape velocity, or they may attain escape velocity through radiation pressure, which imparts an antisunward acceleration. Radiation

pressure is highly dependent on the TAA of Mercury owing to the eccentricity of the orbit about the Sun (e.g., Smyth & Marconi 1995a, 1995b; Schmidt et al. 2010). Atoms that are not lost kinetically can be removed from the exosphere by interactions with the surface, described in Section 2.3.1. They can become photoionized, in which case they can be entrained in the solar wind, entrained in the magnetosphere (and potentially reimpact the surface), or accelerated down the planet's magnetotail. Ejected molecules can be photodissociated or dissociated through electron impacts, which can also impart energies above escape to the resultant atoms (Valiev et al. 2017); molecular dissociation is not considered here because Na is believed to be primarily ejected in the atomic form.

2.3.1. Surface Interaction

Each species reacts with the regolith in a different way. Both source processes and surface interactions are species dependent. Solar wind ions implant themselves into the regolith and cause physical and chemical changes. Physical sputtering and backscattering are relatively high-energy release mechanisms, whereas chemical sputtering, involving chemical reactions between the projectile and target atoms, and thermal processes have lower energies on average. We do not consider chemical sputtering in this paper. We assume that particles are emitted with an isotropic angular distribution. Anisotropic distributions are not supported by the Monte Carlo code at this time. Each emitted particle is followed on all of its ballistic hops until it is lost from the system either to sticking, escape, or photoionization.

When a particle comes back into contact with the surface, there are a variety of processes that can occur. These surface–exosphere interactions in the extreme vacuum environment of airless bodies introduce an array of interesting physics questions that are still not well studied, but can have an effect on the exospheric distribution. When the exospheric particle reencounters the planet, it may stick to the surface, it may adsorb to the surface long enough to partially or fully accommodate (thermalize) to the local surface temperature and then be reemitted, or it may rebound on contact retaining all or most of its incident energy. Each packet is reemitted in a random direction at a speed between the incident speed (v_0) and the local thermal speed (v_{th}) depending on the accommodation factor, a. The new velocity is $v_1 = av_{th} + (1 - a)v_0$. We have used temperature-dependent accommodation, as given by Yakshinskiy & Madey (2005) for Na. In addition, a sticking coefficient, defined to be between 0 and 1, determines the fraction of the packet that sticks when it hits the surface. The sticking coefficient is also temperature dependent (Yakshinskiy & Madey 2005) but we have used the average value (0.5) for simplicity. Our Monte Carlo code is flexible to allow the user to select from this wide range of surface interactions. Comparing the results with different assumptions provides insight into how the surface–exosphere interface affects the exospheric properties. In this work, we assume the surface interaction is temperature-dependent sticking (Yakshinskiy & Madey 2005). Other surface interactions that may be important but which are not considered in our code include diffusion into and out of the surface or along the surface of grains (e.g., Sarantos & Tsavachidis 2020) and dielectric breakdown (Jordan et al. 2019). These processes affect the source maps and will be considered in a future work.

2.3.2. Photoionization

Photoionization rates depend on the ionization potential of the atom in question, and also on the solar flux available with an energy at or exceeding the ionization energy. Most of this energy comes in the form of UV radiation. The solar UV flux is currently available on the LISIRD website (https://lasp.colorado.edu/lisird/). We use the ionization cross sections compiled by Huebner & Mukherjee (2015). The value used is for the quiet Sun scaled to the orbital distance of the planet at the time of observation. The value in Huebner & Mukherjee (2015) is from Verner et al. (1996) compiled in the TOPBase website.

The probability of photoionization during a given ballistic hop is based on the photoionization time (Huebner et al. 1992) and the time of flight in sunlight. If the particle does not escape, the simulation finds the location where the particle reencounters the surface. Photoionization loss rates and seasonal variability at Mercury have been estimated by Jasinski et al. (2021).

3. Mercury's Exosphere

Several parameters of the Monte Carlo code specific to application at Mercury are the temperature function, sticking coefficients, release energy distribution, loss probabilities, and radiation pressure acceleration. Radiation pressure is important for Na, and is highly dependent on heliocentric radial velocity (Potter et al. 2007; Killen et al. 2009a, 2009b).

Our model code outputs a number of measurable exospheric parameters. Possible outputs include exospheric zenith column abundance; line-of-sight column density of exospheric particles; the surface density of particles as they reencounter the surface (including those adsorbed to the cold nightside); and position, density, and specific loss process, whether kinetic escape, photoionization, or sticking on the surface. The code can directly compare the output of the simulation with MESSENGER MASCS data. Comparison of our model results to observations published in Cassidy et al. (2015) are given in Section 5.

3.1. Simulations

The source mechanisms influence the spatial distributions of atoms and their energy distributions. The importance of each source mechanism to different atomic species varies, depending on the volatility of the species and the yield. IS yields vary with mineral type as described previously (e.g., Wehner & Ken-Knight 1967; Roth et al. 1979; Szabo et al. 2018; Morrissey et al. 2022).

3.1.1. Sputtering Yields

When modeling IS from mineral surfaces, a key input parameter is the SBE of the atom being considered. The SBE influences both the sputtering yield and energy/velocity distribution of sputtered particles. The SBEs used in previous models of the Hermean exosphere have varied by nearly an order of magnitude, from 0.27 eV (Wiens et al. 1997; Leblanc & Johnson 2003) to 2.65 eV (Lammer et al. 2003). For ion sputtering from multicomponent substrates, theoretical models typically use the atomic cohesive energy for a monatomic substrate, which is 1.1 eV for Na, but this ignores the potential effects of bonding between the Na with other atoms in the

Table 2
Na Sputtering Yield from 1 keV H^+ on Albite at Normal Incidence vs. SBE Using SDTrimSP

Na SBE (eV)	Source of SBE	Sputtering Yield from Albite at Normal Incidence (atoms/ion)
0.27	Sodium sulfate (Na_2SO_4),	1.15E-2
1.1	Pure Na cohesive energy	6.04E-3
2.6	Na orthosilicate (Na_4SiO_4)	2.09E-3
4.4	Na metasilicate (Na_2SiO_3)	1.00E-3
7.9	Albite ($NaAlSi_3O_8$)	4.12E-4

multicomponent material. The theoretical molecular dynamics (MD) values given in Table 2 for the SBE of Na-bearing silicates from Morrissey et al. (2022) range from 2.6 eV for Na orthosilicate (Na_4SiO_4) to 7.9 eV for albite ($NaAlSi_3O_8$), the latter of which is the Na-bearing feldspar end-member. The Na on the surface of Mercury is believed to be contained in an intermediate-composition feldspar (Peplowski et al. 2014, 2015). Because the Na in feldspar is bonded to the oxygen atoms in the mineral lattice structure and not any other atoms, we expect that the Na SBE for an intermediate Na-bearing feldspar should be essentially identical to that for albite.

The work of Morrissey et al. (2022) demonstrated that the sputtering yield and energy distribution were highly dependent on the Na SBE. However, they did not consider the role of the SBE on predicted exosphere density and dynamics. As such, we have compared Na exospheres simulated using the yield and velocity distribution described as a function of Na SBE from Morrissey et al. (2022) assuming 1 keV H^+ onto albite at normal incidence. Note that 1.1 eV is included in Table 2 for completeness, although we did not simulate models for that particular SBE. We increased the sputtering yield at normal incidence given in Table 2 by one third to account for the average incidence angle of 25° found in the Fast Imaging Plasma Spectrometer (FIPS) data. We used data for 1 keV H^+ on C to estimate the increased yield with incidence angle (Behrisch & Eckstein 2007).

Sputtering yields have been calculated for various assumed SBEs using the binary collision approximation modeling code SDTrimSP as per the methodology by Morrissey et al. (2022). We have used the following SBEs: 0.27, 2.6, 4.4, and 7.9 eV, spanning the values used in previous simulations and calculated by MD for various substrates. First, a series of Na SBE values are obtained based on previous experimental fits (Wiens et al. 1997; Leblanc & Johnson 2003, 2010), approximations (Mutzke et al. 2019), and MD simulations (Morrissey et al. 2022). These values are then used as inputs into SDTrimSP for 1 keV H^+ impacting albite at normal incidence. The density of the albite mineral was assumed to be 2.62 g cm^{-3}. Following Möller & Posselt (2001) and Szabo et al. (2020), the elemental density of oxygen in the albite was modified in SDTrimSP to achieve a bulk density of 2.62 g cm^{-3}, matching experimental data (Mineral Data Publishing 2001). SDTrimSP yields are a function of the percentage of Na in the mineral simulated. Morrissey et al. (2022) simulated albite, which is one-thirteenth Na. Therefore, before we scale by the percentage of Na on the surface we first multiply the results by 13 (to remove the scaling due to albite) and then by 0.05 (5% is the percentage of Na in the Hermean regolith at high latitudes). This Na fraction, along with the assumption of the maximum ion flux measured by the FIPS instrument, means that our sputter yields represent an upper limit. For comparison with the observations of Cassidy et al. (2015) in Section 5, we varied f_{Na} between the observational constraints of 0.02 and 0.05 (Peplowski et al. 2014).

For these simulations, the ion flux to the cusp regions, F_{ion}, is assumed to be the maximum flux given by Raines et al. (2014), which is 6.7×10^8 ions cm^{-2} s^{-1}, scaled by the source map, f_m. The actual flux varies between a minimum value of 9.2×10^3 ions cm^{-2} s^{-1} to the maximum above. Sputtering is assumed to emerge from the areas in the ion precipitation maps, respectively (Figures 1(a) and (b)), with SBEs of 0.27, 2.6, 4.4, and 7.9 eV being used in the simulations. Calculated sputtering yields, y_i, at normal incidence for each SBE are taken from Table 2 and are subsequently scaled for the average incidence angle of the FIPS data. The sputter rate at each pixel is therefore given by

$$R_{sputter} = 1.3\, F_{ion} f_m y_i \sigma n(\mathrm{Na}), \quad (4)$$

where F_{ion} is the assumed FIPS-derived value, f_m is the value (between 1 and 0) of the sputter map at the pixel in question, y_i is the sputter yield for the assumed SBE, σ is the surface number density (7.4×10^{14} atoms cm^{-2}) and n(Na) is the fractional sodium abundance, taken to be 0.05 in the cusp regions. The yield at normal incidence was increased by a factor of 1.3 to take into account the average angle of incidence of the ions at the surface.

3.1.2. Source Maps

We have calculated surface source maps for our assumed source processes: IS (Figures 1(a) and (b)), IV, and PSD (Figure 1(c)). For this study, we use the measured cusp region in the northern hemisphere from the FIPS instrument on MESSENGER (Raines et al. 2014) to represent the IS contribution. We assume that the southern cusp is at a slightly lower latitude in the southern hemisphere (10° closer to the equator) than in the north, but has the same ion flux as in the north. The lower latitude in the south is to account for Mercury's offset magnetic dipole (Anderson et al. 2012; Fatemi et al. 2020); however, the exact placement and assumed flux (relative to the north) do not significantly change the conclusions reached here, which are primarily to explain the observability of sputtering as a function of SBE over the exosphere generated by other processes. The maximum flux was chosen to place an upper limit on observability. Two IV cases are simulated corresponding to the lower and upper limits for IV from Mouawad et al. (2011). We have parameterized the impact flux from the surface as having a Gaussian distribution centered on the dawn equator following the model of Burger et al. (2012, 2014) that provided an excellent fit to MESSENGER MASCS calcium data. We define each point on the surface by its longitude, λ, and latitude, μ, relative to the subsolar point, where $\lambda = 0$ is the subsolar meridian, $\lambda = \pi/2$ is the dusk meridian, and the latitude varies from $-\pi/2$ at the

Table 3
Derived Scale Heights for the Various Exospheric Processes

Source Process	Scale Height (km)
PSD	72
IV (upper limit)	340
IV (lower limit)	340
IS (SBE = 0.27 eV)	390
IS (SBE = 2.6 eV)	650
IS (SBE = 4.4 eV)	860
IS (SBE = 7.9 eV)	1460

south pole to $\pi/2$ at the north pole. In Mercury Solar Orbital coordinates, a unit sphere is defined by the radius vector from the planet's center, r, defined by

$$r(x; y; z) = (\cos\lambda\cos\mu, \sin\lambda\cos\mu, \sin\mu). \quad (5)$$

The flux at each point on the surface is then given by

$$f(\lambda, \mu) = f_0 \exp(-\phi(\lambda, \mu)/\sigma g), \quad (6)$$

$$\cos\phi = r \cdot r_0, \quad (7)$$

where f_0 is the maximum flux from the surface, σ_g is the angular width of the source, and r_0 is a vector from Mercury's center to source center (see Section 2.2.2). These models assume a source centered at the dawn, equatorial point [$(\lambda, \mu) = (-\pi/2, 0)$].

For PSD, Na atoms are chosen according to the fractional PSD yield at each surface element. The details and justification for the PSD source map are discussed in Section 2.2.1.

4. Comparisons of the Different Source Processes

Our primary goal in this paper is to illustrate the effect of SBE on the sputtered component of the exosphere, and to illustrate how sputtering can be differentiated from the other various source processes known to be active in promoting Na to Mercury's exosphere. The scale heights for the various processes are summarized in Table 3. Miscellaneous parameters in these runs are given in Table 1. All the simulations have been run at a Mercury TAA = 26° except those specifically run for comparison with the results shown in Figure 6 of Cassidy et al. (2015). That profile corresponds to a TAA of 144° on 2012 June 29 (corrected date, private communication). The choice of TAA 26° represents a time in Mercury's orbit when solar flux, surface temperatures, and radiation pressure were all at intermediate values. This should allow the signatures of each process to be more readily discerned as we have avoided times when weak or strong radiation pressure blends the signatures on the dayside and nightside/tail regions, respectively. The reemission of emitted particles that return to the planet's surface is isotropic. Sputtering parameters (Table 2) are taken for normal incidence of ions but, taking into account the average angle for the incident ions, we used a yield that has been increased by 30% to take into account the average angle for the incident ions (Behrisch & Eckstein 2007). Simulations are performed for IS, IV, and PSD separately and subsequently added for the various illustrations to show the dominance of one source over another in various regions about the planet.

The simulations in Figure 2 offer a graphical comparison of the results for SBE 0.27–7.9 eV, including IS from the northern cusp only, as shown in Figure 1(a). As the SBE increases, the tail region is much less populated by IS, the density decreases throughout the near-cusp region, and there is less Na in the hemisphere opposite the cusp. The simulations in Figure 2 convey the two important differences between IS-derived exospheres assuming different SBEs: yield and energy distribution. Figure 2(a) assumes the lowest SBE considered, 0.27 eV, for which the yield is greatest and the ejecta energy is least. About 30% of the ejected Na atoms directly escape for this case. The remainder can reimpact the surface or they can be accelerated antisunward by radiation pressure, contributing to the tail in the hemisphere opposite from the originating cusp. Figure 2(b) shows the results for the same cusp region using SBE = 2.6 eV, Figure 2(c) is the simulation with SBE = 4.4 eV, and Figure 2(d) shows the simulation with SBE = 7.9 eV. A gradual change is seen as the yield decreases and the ejecta energy increases with increasing SBE. Ninety-five percent of those atoms ejected from the cusp regions assuming a SBE of 7.9 eV (Figure 2(d)) will directly escape from the planet's gravitational field (Morrissey et al. 2022), tracing nearly linear trajectories away from the planet. They will not be seen tailward in the hemisphere opposite from the source cusp, as contrasts with the case of the lowest SBE. Because the simulations assume the maximum flux from Raines et al. (2014), IS can be much less at any given time. It can also be larger during times when the entire dayside surface may be open. Sputtering will scale as the solar wind flux and the surface area open to precipitation.

The flux of escaping Na atoms actually peaks for SBE values of ~1 eV, owing to the combined effects of IS yield and ejecta energy distribution (Morrissey et al. 2022). Figure 2(a) most clearly illustrates that the atoms contributing to the antisunward tail gain the energy to escape by radiation pressure acceleration, as we now explain. In Figure 2(a) particle trajectories are seen to curve from the cusp region around the planet to the downtail region. Those atoms ejected with escape velocity contribute to a dayside corona, as seen in Figure 2(d). Those atoms accelerated to escape velocity by radiation pressure contribute to the antisunward tail. The low-energy portion of the velocity distribution, most dominant for the low SBE values, contributes to a dayside exosphere with a small scale height. The presence of a strong tail asymmetry in the opposite hemisphere from the open cusp could be a diagnostic of a low SBE at Mercury if the Na exosphere is observed during the appropriate solar wind conditions where only one cusp is open.

The scale height for sputtering increases with greater SBE (Figure 3), but above 1000 km from the surface of the planet, the altitude distribution for all SBE values converge to that for an escaping exosphere. Measurements of the Na line-of-sight column density and spatial distribution would be most useful in distinguishing the IS component of the exosphere given the range in scale heights among the IS, PDS, and IV processes, as we discuss below.

The simulations shown in Figure 4 result from IV only assuming (a) the lower limit for IV and (b) the upper limit for IV from Mouawad et al. (2011) for a dawn-centered Gaussian spot described earlier. Φ^{IV} at the spot center is assumed to be $1. \times 10^5$ cm^{-2} s^{-1} at minimum and 2.1×10^6 cm^{-2} s^{-1} at maximum at a heliocentric distance of 0.354 au. The IV is scaled from these values by $(0.352/R_h)^2$. We assumed a Maxwellian velocity distribution at a temperature of 3500 K (Killen et al. 2019) leading to the same scale height of 340 km for the lower and upper limits assumed for IV. The assumed

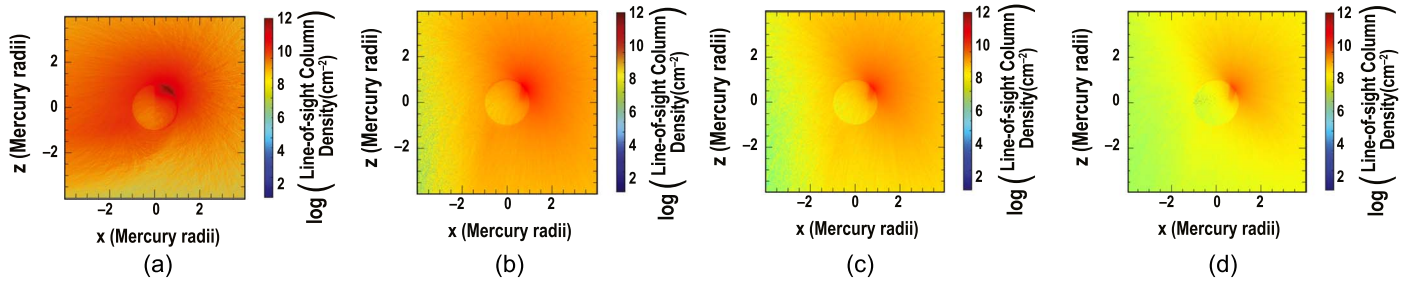

Figure 2. These simulations trace the gradual change in the exosphere derived from IS, from the northern cusp only, assuming SBEs of (a) 0.27 eV, (b) 2.6 eV, (c) 4.4 eV, and (d) 7.9 eV. The $+x$-axis is toward the Sun and $+z$ is northward. Column density is the cumulative number of atoms cm^{-2} along the line of sight in the y-axis direction, which runs dawn–dusk and is perpendicular to the page.

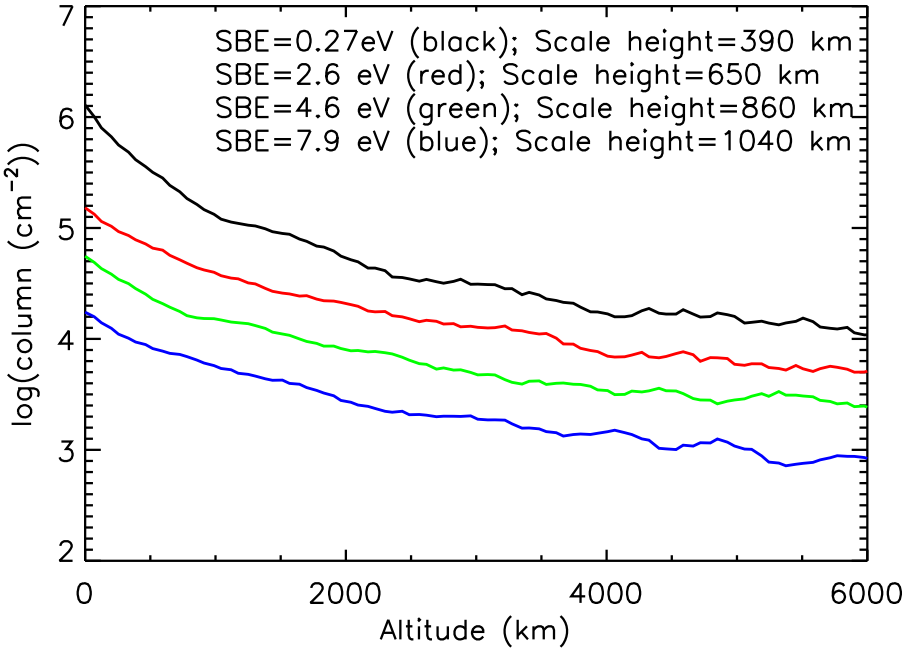

Figure 3. Altitude profiles measured radially from the planet directly above the center of the cusp at a latitude of 67°N. Four values of SBE were assumed: 0.27, 2.6, 4.4, and 7.9 eV. The plots have been smoothed, but the high altitudes still appear wavy owing to poor statistics. Above about 1000 km the curves asymptote because all trajectories are escaping.

temperature of the IV component is based on the hypervelocity impact experiments of Schultz et al. (2007). They performed laboratory experiments to infer vapor temperatures of a self-luminous vapor cloud, and obtained temperatures of 3900 K for gas comprised of CO or 4200 K for gas comprised of individual atoms. Because these are initial temperatures from the impact during the luminous phase, and analysis suggests significant radiative cooling in the first 10 μs (Collette et al. 2013), we assumed a slightly lower temperature. Measured scale heights at any given location above the planet's surface depend not only on the source but also on radiation pressure and gas–surface interaction. The total escape rate of IV-generated ejecta from the planet is dependent on the micrometeoroid flux and velocity, as well as radiation pressure, all of which depend on TAA. Variations in the interplanetary dust density and velocity along Mercury's orbit result from the ellipticity and orbital inclination of the orbit. Both the initial ejecta velocity and radiation pressure acceleration can provide escape velocity for many of the atoms ejected by IV. The exact escape rate depends on the radiation pressure.

In the simulations in Figure 5, the results of the minimum IV case are combined with IS simulations that include both a northern and southern cusp. The IS component is definitely discernible and prominent above IV for the minimum IV flux (compare to Figure 4(a)). IV produces a prominent antisunward tail with a different spatial distribution than that from the IS component. For the case of maximum IV (compare to Figure 4(b)), the IS component would most clearly be observable on the sunward side of the planet above approximately a planetary radius from the surface.

The simulation of an exosphere with PSD only is shown in Figure 6(a), where the surface map from which the ejected atoms are chosen is illustrated in Figure 1(c). The maximum line-of-sight tangent column density in this simulation is $\sim 2.1 \times 10^{12}$ cm^{2} at the subsolar point. The corresponding surface number density is approximately 1.8×10^{4} cm^{-3} using Equation (7.1.63) from Chamberlain & Hunten (1987). This equation assumes a uniform exosphere and is thus not strictly correct. The column density tangent to the surface at midnight is $\sim 1.5 \times 10^{11}$ cm^{-2}. Although the source rate for PSD is much greater than that for the other processes, its dayside scale height is low, about 72 km (Figure 6(a)). This is only one quarter that of IV and about 5% that for IS with a SBE of 7.9 eV. Figure 2 shows that the IS-generated exosphere creates a corona about the planet that is not seen for PSD. Almost no Na resulting from PSD can be seen greater than one Mercury radius from

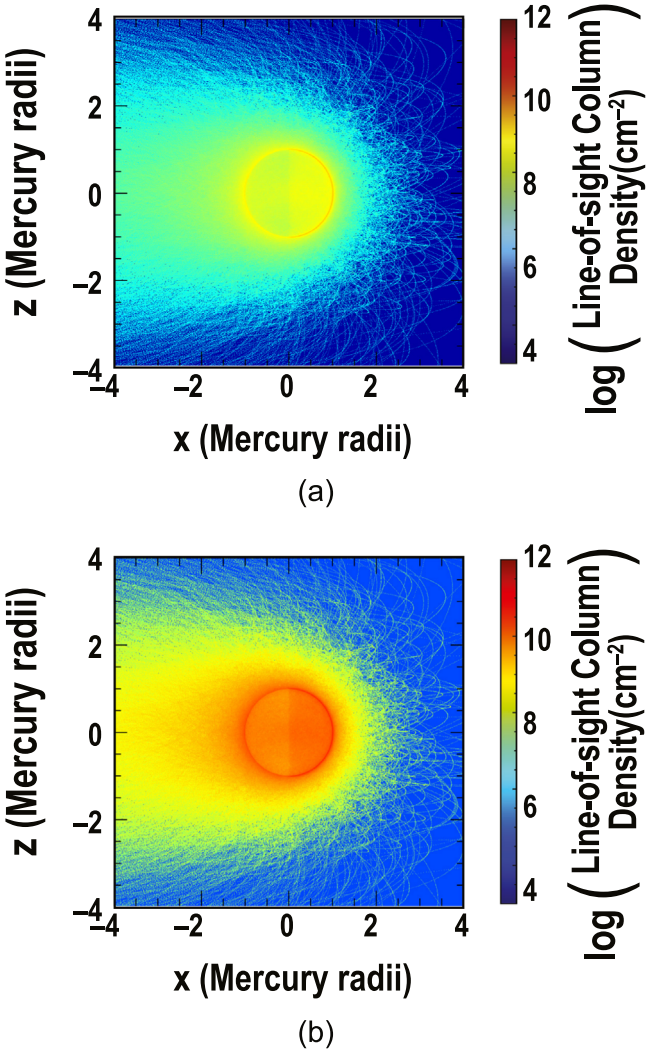

Figure 4. The IV-generated exosphere is simulated for the (a) lower limit and (b) upper limit from Mouawad et al. (2011). The image is seen from the dawn hemisphere centered on the terminator. The Sun is to the right and north is up.

the dayside surface in this simulation, in contrast with all of the simulations for IS and IV. In addition, the tail is much wider from PSD than from IV (compare Figures 4 and 6) and could be used as a diagnostic of the source(s).

Comparisons of this PSD-only exosphere to the combination of the maximum IV simulation with the northern-cusp-only IS simulations for SBE = 0.27 eV and 7.9 eV are shown in Figures 6(b) and (c), respectively. It is instructive to compare with Figure 5, which shows the comparison for all four SBE values with the minimum IV case. The IS cusps can clearly be seen above the IV for the minimum IV scenario. Figures 6(b) and (c), on the other hand, illustrate the influence of the maximum IV rate on the observability of the IS-derived component of the overall Na exosphere. Although the IS component is observable for the lowest SBE for both assumed IV rates, when the SBE is high, as we expect for the Na-bearing minerals of Mercury's surface (Morrissey et al. 2022), the IS component is much more difficult to discern from the maximum IV-derived component. It also illustrates the influence of an asymmetry in the IS-derived Na if, for instance, only one cusp is open to the solar wind. This is seen most dramatically in Figures 6(b) and (c). The IS component is observed in the dayside hemisphere above the open cusp but not in the antisolar hemisphere for SBE = 7.9 (Figure 6(c)). For the case with the lower SBE, the asymmetry is seen both in the dayside hemisphere and in the antisolar hemisphere opposite to the open cusp (Figure 6(b)).

5. Comparisons with Data

A limited subset of the MESSENGER MASCS sodium data set was published by Cassidy et al. (2015). Here we compare subsolar limb profiles from our simulations of PSD, IV, and IS for the minimum and maximum SBE (0.27 and 7.9 eV) with the noon local time limb profile presented in Cassidy et al. (see upper-right panel of their Figure 6). That profile corresponds to a TAA of 144° on 2012 June 29 (corrected date, private communication), so our comparisons were simulated for that TAA. For these simulations we also assumed a source temperature of 5000 K for IV, consistent with the Cassidy et al. results regarding possible IV contributions.

Figure 7 shows the comparisons of our models to these MESSENGER data. The data shown by the black circles are the MESSENGER MASCS subsolar limb scans. The green regions indicate the range of PSD altitude profiles, with the lower edge corresponding to a reduced PSD cross section of 1×10^{-20} cm^2 and $f_{\rm Na} = 0.02$ (which we take as lower bounds of both parameters in our models, as discussed above), and the upper edge corresponding to the measured PSD cross section of 3×10^{-20} cm^2 and $f_{\rm Na} = 0.05$ (which we take as upper bounds of both parameters, also discussed above). The orange regions indicate the range of IV altitude profiles, with the lower edge corresponding to the minimum IV case (1×10^5 cm^{-2} s^{-1}) and the upper edge to the maximum IV case (2.1×10^6 cm^{-2} s^{-1}) both estimated at 0.352 au from Mouawad et al. (2011). IV is always scaled as R_h^{-2}. The blue curves indicate the sum of the altitude profiles from IS in both the north and south cusps for SBE = 0.27 eV (a) and SBE = 7.9 eV (b) and and an assumed flux equal to the MESSENGER FIPS-measured maximum (6.7×10^8 ions cm^{-2} s^{-1}; Raines et al. 2014). The red curves are example combinations of PSD, IV, and IS that match the data. The red curve in Figure 7(a) is the sum of PSD for the enhanced cross section and $f_{\rm Na} = 0.04$, IV for the maximum case, and 0.03 times the blue curve for the IS contribution (i.e., a flux of 2.0×10^7 ions cm^{-2} s^{-1}).

The red curve in Figure 7(b) is the sum of PSD for the measured cross section and $f_{\rm Na} = 0.04$, IV for the maximum case, and the blue curve for the IS contribution assuming SBE = 7.9 eV.

One clear implication of our results shown in Figure 7 is that PSD is the dominant contributor to the exosphere at low altitudes. The large scale heights for IV and IS cannot match the scale height of the data at lower altitudes; PSD must be the dominant process at those altitudes. Although the PSD yields measured by Yakshinskiy & Madey (1999) were reduced by a factor of three in previous models to $Q = 1 \times 10^{-20}$ cm^2, as suggested by Cassidy & Johnson (2005), the comparison to the data here suggests that the measured cross section, 3×10^{-20} cm^2, is needed to match the data, along with $f_{\rm Na} = 0.04$, a reasonable number fraction bracketed by the measured equatorial value of 0.02 and the value of 0.05 for the northern plains (Peplowski et al. 2014). At low altitudes, there is still a slight difference in scale height between the simulations and the data, which may indicate that the temperature for PSD is

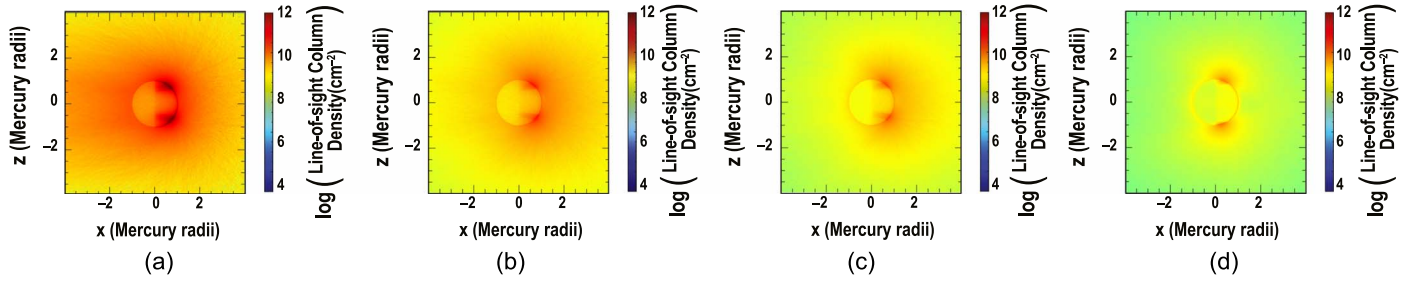

Figure 5. Comparison of the combination of IS (from both the northern and southern cusp) and IV, in which the simulation in Figure 4 for minimum IV flux has been added to IS exospheres for SBEs of (a) 0.27 eV, (b) 2.6 eV, (c) 4.4 eV, and (d) 7.9 eV. These illustrate where and to what extent the two processes can be distinguished.

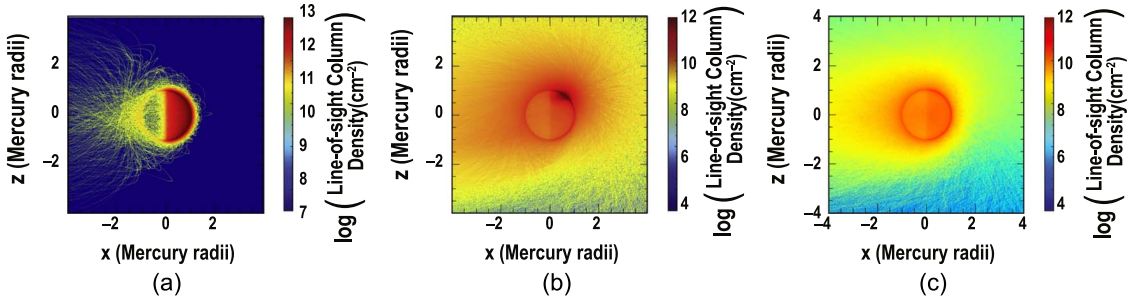

Figure 6. (a) PSD seen from the dawn equatorial terminator. (b) Maximum IV spot at dawn combined with IS at the northern cusp only and SBE = 0.27 eV. This provides an illustration of a single cusp being open to the solar wind. (c) Same as (b) but with SBE = 7.9 eV.

slightly higher than the assumed value of 1200 K, but the overall match between the PSD simulations and the data at low altitudes is good.

The second implication of our results is that the data at high altitudes can only be matched by IV, IS, or a combination of the two; the scale height for PSD is too small to match the observations at higher altitudes. The maximum IV range falls just below the data in this example, suggesting that IV could potentially be the sole source of the Na at the higher altitudes in some cases. Given that the sum of this maximum IV and the blue IS contribution for SBE = 7.9 eV (Figure 7(b)) brings the profile up to match the data well, we can conclude that SBE = 7.9 eV is consistent with observations as long as the IV contribution is on the high end of the simulations and the particle flux is on the order of the higher fluxes measured by MESSENGER FIPS. In contrast, the high-altitude portion of the blue IS contribution for SBE = 0.27 eV (Figure 7(a)) is roughly an order of magnitude too high compared to the data. The only way for IS with SBE = 0.27 eV to be consistent with the observations is for the assumed particle flux to be significantly reduced (the simulations are for the MESSENGER FIPS maximum flux of 6.7×10^8 ions cm^{-2} s^{-1}; Raines et al. 2014), for the IV contribution to be at the low end of the simulated range, or for the profile to be a combination of an intermediate IV contribution and a reduced particle flux for the IS contribution. In Figure 7(a) (SBE = 0.27) the red curve match to the data was achieved by reducing the particle flux to 3% of the MESSENGER FIPS maximum while keeping the IV contribution corresponding to the maximum IV case. However, we can largely rule out the SBE = 0.27 eV fit based on the minimal seasonal variation seen in the Na exosphere, as we now explain.

The third implication of our data–model comparisons in Figure 7 is that a Na SBE = 0.27 eV appears to be unlikely. There is little variation in the Na at a given TAA over seven Mercury years of observations, as is shown in Figures 4 and 5 of Cassidy et al. (2015). This year-to-year repeatability, or seasonality, of the Na observations is also seen in Ca and Mg observed by MESSENGER (Burger et al. 2012, 2014; Merkel et al. 2017). PSD and IV both essentially vary as a function of Mercury's TAA, being largely a function of R_h; therefore, they are seasonal in their variation and one can expect a similar contribution at a given TAA year after year (e.g., Cassidy et al. 2015). As we can see in Figure 7, PSD dominates at the low altitudes, so the seasonality in Figure 5 of Cassidy et al. (2015), which was generated for data at an altitude of 300 km, is understood. In our model shown in Figure 7, although it falls a little short of the data at high altitudes, IV provides a stable, seasonally varying base for the profiles at high altitudes that could easily explain the repeatability of the high-altitude profiles in Figure 4 of Cassidy et al. In contrast, IS varies with the space environment, which is constantly changing in a more or less random manner. Because IS is undoubtedly occurring, it likely does contribute some additional Na at the high altitudes, but at levels that are small and not leading to large variations from year to year. This level of contribution is consistent with the SBE = 7.9 eV case shown in Figure 7(b). If the Na SBE were 0.27 eV, however, then IS would dominate over IV at times by at least an order of magnitude; such variability in the IS contribution would be readily detectable in the MESSENGER data but was not observed. Furthermore, any large variability in the IS contribution for SBE = 0.27 eV would have to be balanced by an equally large variability in the IV contribution. Such exactly offsetting changes between IS and IV to keep the net Na exosphere at high altitudes repeatable from year to year are unphysical. Therefore, such a low SBE is unlikely to be consistent with the observations of year-to-year repeatability.

The same argument can be employed for combinations of IV and IS for other values of SBE. It will likely always be

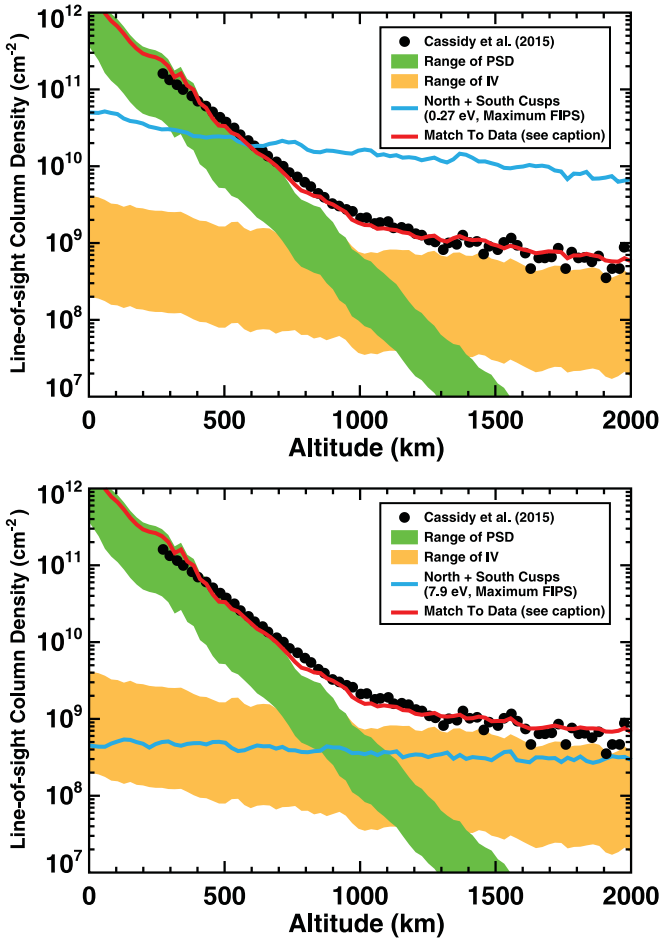

Figure 7. Comparisons of our models to MESSENGER data. The column density shown is an integrated line-of-sight value, not a zenith column. The data (black circles) are subsolar MESSENGER MASCS limb scan data at TAA 144° from Cassidy et al. (2015; upper-right panel of their Figure 6). The green regions indicate the range of PSD altitude profiles, with the lower edge corresponding to a PSD cross section of 1×10^{-20} cm^2 and $f_{Na} = 0.02$ (which we take as lower limits of both parameters), and the upper edge corresponding to the measured PSD cross section of 3×10^{-20} cm^2 and $f_{Na} = 0.05$ (we take as upper limits of both parameters). The orange regions indicate the range of IV altitude profiles, with the lower edge corresponding to the minimum IV case (1×10^5 cm^{-2} s^{-1}) and the upper edge to the maximum IV case (2.1×10^6 cm^{-2} s^{-1}) at 0.352 R_h of Mouawad et al. (2011). IV is always scaled as R_h^{-2}. The blue curves indicate the sum of the altitude profiles from IS in both the north and south cusps for SBE = 0.27 eV (a) and SBE = 7.9 eV (b) with an assumed flux equal to the MESSENGER FIPS-measured maximum (6.7×10^8 ions cm^{-2} s^{-1}; Raines et al. 2014). The red curves are example combinations of PSD, IV, and IS that match the data (see text for discussion). The red curve in (a) is the sum of PSD for the enhanced cross section and $f_{Na} = 0.04$, IV for the maximum case, and 0.03 times the blue curve for the IS contribution (i.e., a flux of 2.0×10^7 ions cm^{-2} s^{-1}). The red curve in (b) is the sum of PSD for the enhanced cross section and $f_{Na} = 0.04$, IV for the maximum case, and the blue curve for the IS contribution.

possible to adjust the IV flux to levels consistent with an IS flux that is somewhere in the observed range from MESSENGER FIPS and thus match the high-altitude observations. However, the FIPS-observed fluxes range over *four orders of magnitude*, which would require significant and large compensating variations in the IV flux at any given instant. This is unphysical and inconsistent with MESSENGER MASCS observations of Ca that are well fit by an IV-dominated source and show year-to-year repeatability at a given TAA (Burger et al. 2012, 2014). This therefore suggests that a high value for the SBE is favored, for which the IS contributions range from small to negligible and IV is the dominant high-altitude source process.

Note that these comparisons to MESSENGER data are only to establish that the simulations we present are a reasonable representation of Mercury's exosphere. The main goal of this paper is to illustrate how the SBE affects the IS contributions to the exosphere, to place IS in context with the other dominant processes that form the exosphere, and to provide a framework for suggesting where observations of the exosphere are likely to provide the best diagnostics of the various processes.

The scale height of the IS contribution, and therefore the altitudes at which the IS contribution is observable, is a direct result of the assumed binding energies. The scale height progressively increases as the SBE increases, but at the same time the yield decreases with increasing SBE. However, because the Na scale height also changes away from any given source region, owing to radiation pressure and surface interactions, one cannot always attribute the combined scale height to any of the individual source processes. A three-dimensional model including all source processes, compared with data, is thus required to determine the relative contribution of the various sources to the exosphere.

In this work, we have used such a model to simulate the contributions of IS, IV, and PSD to Mercury's exosphere and thus illustrate the manner in which the IS contribution changes with the SBE in relation to the more stable and repeatable contributions (for a given TAA) from IS and PSD. As shown in Figures 2–6, there are certain regions of the exosphere about the planet where a given process is more likely to dominate depending on the SBE; therefore, these are the regions where observations are the most diagnostic. Simulations such as those presented here can guide the analysis of existing data and serve as a roadmap for future observations.

6. Conclusions

We have simulated Mercury's exosphere using the source processes PSD, IV, and sputtering with SBEs of 0.27, 2.6, 4.4, and 7.9 eV, ranging from the lowest value SBE commonly used in exosphere models to the highest value from recent molecular dynamics calculations for the Na-bearing feldspar end-member, albite. We find that the processes responsible for generating Mercury's Na exosphere are separable by measuring line-of-sight column densities tangent to the planet at various altitudes and positions around the planet. The low-altitude exosphere is dominated by PSD, and the altitudes above ~1000 km are dominated by IV. We conclude that high-altitude data (>1000 km above the surface) are consistent with a small portion of the Na being sputtered from a high-SBE material such as feldspar, which has been predicted to be abundant on Mercury's surface, and that the SBE for that surface is generally consistent with values on the order of 7.9 eV. That means that IS contributes a small, but potentially measurable, contribution at high altitudes, along with the IV component.

In summary, our results favor a high SBE. Technically, any SBE can work for IS at high altitudes if the IV is reduced to allow for it. However, that means the IS would have to follow the same seasonal trends as IV—but in the opposite sense—for the observed year-to-year repeatability to be possible; this is especially so when the SBE is low and the IS component is

much more sensitive to changes in the IS flux. This seasonal variation of IS is unphysical. IS is due to the solar wind and should vary much more randomly than IV. There is no reason to expect that IS would vary in the opposite direction to IV at all times. Because of this required interplay between IV and IS, a high SBE is favored as the variations in IV would not need to be offset by the IS to nearly as large a degree as they would for a low SBE, if at all, given that IV is repeatable from year to year. This suggests that for the high-altitude component of Mercury's Na exosphere IS is a small contribution on top of a primarily dominant IV component.

We are currently expanding our study to include all of the MESSENGER Na data, which will allow for greater constraints on the various model parameters as a function of location about the planet and TAA.

We thank two anonymous referees for suggestions that substantially improved the manuscript. We acknowledge support from NASA Solar System Workings Award, grant Nos. 80NSSC18K0521 and 80NSSC22K0099. R.M.K. and L.S.M. were partially supported by the NASA Solar System Exploration Research Virtual Institute team, LEADER. O.J.T. was supported by the GSFC ISFM. R.J.V., R.M.K. and M.H.B. were partially supported by NASA DDAP Award 80NSSC18K0352.

Software: The source code for the Monte Carlo model is publicly available at https://github.com/mburger-stsci/nexoclom.

ORCID iDs

Rosemary M. Killen https://orcid.org/0000-0002-0543-2326
Liam S. Morrissey https://orcid.org/0000-0001-7860-9957
Matthew H. Burger https://orcid.org/0000-0002-9334-7198
Ronald J. Vervack, Jr. https://orcid.org/0000-0002-8227-9564
Orenthal J. Tucker https://orcid.org/0000-0002-8235-5440
Daniel W. Savin https://orcid.org/0000-0002-1111-6610

References

Anderson, B. J., Johnson, C. L., Korth, H., et al. 2012, JGRE, 117, E00L12
Arnold, J. R. 1979, JGR, 84, 5659
Aumayr, F., & Winter, H. 2004, RSPTA, 362, 77
Behrisch, R., & Eckstein, W. 2007, Sputtering by Particle Bombardment (Berlin: Springer), 103
Burger, M., Killen, R. M., Vervack, R. J., Jr., et al. 2010, Icar, 209, 63
Burger, M. H., Killen, R. M., McClintock, W. E., et al. 2012, JGRE, 117, E00L11
Burger, M. H., Killen, R. M., McClintock, W. E., et al. 2014, Icar, 238, 51
Butler, B. J. 1997, JGR, 102, 19283
Cassidy, T. A., & Johnson, R. E. 2005, Icar, 176, 499
Cassidy, T. A., Merkel, A. W., Burger, M. H., et al. 2015, Icar, 248, 547
Cassidy, T. A., Schmidt, C. A., Merkel, A. W., et al. 2021, PSJ, 2, 175
Chamberlain, J. W., & Hunten, D. M. 1987, Theory of Planetary Atmospheres (2nd ed.; New York: Academic)
Chang, J.-J., & Kelly, H. 1975, PhRvA, 12, 92
Cintala, M. J. 1992, JGR, 97, 947
Collette, A., Drake, K., Moker, A., et al. 2013, P&SS, 89, 58
Combi, M. R., Disanti, M. A., & Fink, U. 1997, Icar, 130, 336
Crider, D. H., & Vondrak, R. R. 2000, JGR, 105, 26773
Eckstein, W. 2007, in Sputtering by Particle Bombardment, Topics in Applied Physics, ed. R. Behrisch & W. Eckstein, Vol. 10 (Berlin: Springer), 33
Farrell, W. M., Hurley, D. M., Esposito, V. J., et al. 2015a, LPI Contribution, 1878, 2037
Farrell, W. M., Hurley, D. M., Poston, M. J., et al. 2016, AdSpR, 58, 1648
Farrell, W. M., Hurley, D. M., & Zimmerman, M. I. 2015b, Icar, 255, 116
Fatemi, S., Poppe, A. R., & Barabash, S. 2020, JGRA, 125, e27706
Hijazi, H., Bannister, M. E., Meyer, H. M., III, et al. 2014, JGRA, 119, 8006
Hijazi, H., Bannister, M. E., Meyer, H. M., III, et al. 2017, JGRE, 122, 1597
Hodges, R. R. 1973, JGR, 78, 8055
Hofer, W. O. 1991, in Sputtering by Particle Bombardment III, ed. R. Behrisch & K. Wittmaack (New York: Springer), 15
Horanyi, M., Szalay, J. R., Kempf, S., et al. 2015, Natur, 522, 324
Huebner, W. F., Keady, J. J., & Lyon, S. P. 1992, Ap&SS, 195, 1
Huebner, W. F., & Mukherjee, J. 2015, P&SS, 105, 11
Hunten, D. M., Cremonese, G., Sprague, A. L., et al. 1998, Icar, 136, 298
Ip, W.-H. 1993, ApJ, 418, 451
Janches, D., Berezhnoy, A. A., Christou, A. A., et al. 2021, SSRv, 217, 50
Jasinski, J. M., Cassidy, T. A., Raines, J. M., et al. 2021, GeoRL, 48
Jia, X., Slavin, J. A., Poh, G., et al. 2019, AGUFM, SM51A-03
Jordan, A. P., Stubbs, T. J., Shustermand, M. L., et al. 2019, Icar, 319, 785
Kabin, K., Gombosi, T. I., DeZeeuw, D. L., & Powell, K. G. 2000, Icar, 143, 397
Kallio, E., & Janhunen, P. 2003a, GeoRL, 30, 1877
Kallio, E., & Janhunen, P. 2003b, AnGeo, 21, 2133
Killen, R. M., Burger, M. H., Vervack, R. J., Jr., & Cassidy, T. A. 2019, in Mercury: The View after MESSENGER, ed. S. C. Solomon, L. R. Nittler, & B. J. Anderson (Cambridge: Cambridge Univ. Press)
Killen, R., Cremonese, G., Lammer, H., et al. 2007, SSRv, 132, 433
Killen, R. M., Hurley, D. M., Farrell, W. M. & the DREAM Team 2012, JGR, 117
Killen, R. M., & Ip, W.-H. 1999, RvGeo, 37, 361
Killen, R. M., Potter, A. E., Reiff, P., et al. 2001, JGR, 106, 20509
Killen, R. M., Shemansky, D. E., & Mouawad, N. 2009a, ApJS, 181, 351
Killen, R. M., Shemansky, D. E., & Mouawad, N. 2009b, ApJS, 182, 667
Korth, H., Anderson, B. J., Gershman, D. J., et al. 2014, JGRA, 119, 2917
Krachner, A., Aumayr, F., Sears, D. W. G., & Kareev, M. 2003, M&PSA, 38, 5204
Lammer, H., Wurz, P., Patel, M. R., et al. 2003, Icar, 166, 238
Leblanc, F., & Johnson, R. E. 2003, Icar, 164, 261
Leblanc, F., & Johnson, R. E. 2010, Icar, 209, 280
Madey, T. E., Yakshinskiy, B. V., Ageev, V. N., & Johnson, R. E. 1998, JGR, 103, 5873
Mangano, V., Massetti, S., Mililli, A., et al. 2015, P&SS, 115, 102
Mangano, V., Milillo, A., Mura, A., et al. 2007, P&SS, 55, 1541
McGrath, M. A., Johnson, R. E., & Lanzerotti, L. J. 1986, Natur, 323, 694
Merkel, A. W., Cassidy, T. A., Vervack, R. J., et al. 2017, Icar, 281, 46
Mineral Data Publishing 2001, RRUFF, Albite, https://rruff.info/doclib/hom/albite.pdf
Möller, W., & Posselt, M. 2001, TRIDYN_FZR User Manual, (Dresden: FZR), https://d-nb.info/1220294489/34
Morgan, T. H., Zook, H. A., & Potter, A. E. 1988, Icar, 75, 156
Morrissey, L. S., Tucker, O. J., Killen, R. M., et al. 2022, ApJL, 925
Mouawad, N., Burger, M. H., Killen, R. M., et al. 2011, Icar, 211, 21
Mutzke, A., Schneider, R., Eckstein, W., et al. 2019, SDTrimSP Version 6.00, Max-Planck-Institut für Plasmaphysik, doi:10.17617/2.3026474
Nittler, L. R., Starr, R. D., Weider, S. Z., et al. 2011, Sci, 333, 1847
Ohtake, M., Matsunaga, T., Yokota, Y., et al. 2010, SSRv, 154, 57
Peplowski, P. N., Evans, L. G., Stockstill-Cahill, K. R., et al. 2014, Icar, 228, 86
Peplowski, P. N., Lawrence, D. J., Feldman, W. C., et al. 2015, Icar, 253, 346
Potter, A. E., Killen, R. M., & Morgan, T. H. 2000, JGR, 105, 15073
Potter, A. E., Killen, R. M., & Morgan, T. H. 2007, Icar, 186, 571
Potter, A. E., & Morgan, T. H. 1990, Sci, 248, 835
Press, W. H., Teukolsky, S. A., Vetterling, W. T., & Flannery, B. P. 2007, Numerical Recipes: The Art of Scientific Computing (3rd ed.; Cambridge: Cambridge Univ. Press), 1235
Raines, J. M., Gershman, D. J., Slavin, J. A., et al. 2014, JGRA, 119, 6587
Roth, J. 1983, Sputtering by Particle Bombardment II (Berlin: Springer), 91
Roth, J., Bohdansky, J., Blewer, R. S., & Ottenberger, W. 1979, Data on Low Energy Light Ion Sputtering (Garching: Max-Planck-Inst. fur Plasmaphysik)
Sarantos, M., Killen, R. M., & Kim, D. 2007, P&SS, 55, 1584
Sarantos, M., Killen, R. M., Sharma, A. S., & Slavin, J. A. 2008, GeoRL, 35, L04105
Sarantos, M., & Tsavachidis, S. 2020, GeoRL, 47, e88930
Schmidt, C. A., Wilson, J. K., Baumgardner, J., & Mendillo, M. 2010, JGR, 117, A03301
Schultz, P. H., Eberhardy, C. A., Ernst, C. M., et al. 2007, Icar, 191, 84
Slavin, J., Middleton, H. R., Raines, J. M., et al. 2019, JGRA, 124, 6613
Smyth, W. H., & Marconi, M. L. 1995a, ApJ, 441, 839
Smyth, W. H., & Marconi, M. L. 1995b, ApJ, 443, 371
Solomon, S. C., McNutt, R. L., Jr., Gold, R. E., & Domingue, D. L. 2007, SSRv, 131, 3

Stern, S. A. 1999, RvGeo, 37, 453
Sugita, S., Schultz, P. H., & Adams, M. A. 1998, JGR, 103, 119427
Szabo, P. S., Biber, H., Jaggi, N., et al. 2020, ApJ, 891, 100
Szabo, P. S., Chiba, R., Biber, H., et al. 2018, Icar, 314, 98
Valiev, R. R., Berezhnoy, A. A., Sidorenko, A. D., et al. 2017, P&SS, 145, 38
Verner, D. A., Ferland, G. J., Korista, K. T., & Yakovlev, D. G. 1996, ApJ, 465, 487
Von Steiger, R. N., Schwandron, N. A., Fisk, L. A., et al. 2000, JGR, 105, 27217
Wehner, G., & KenKnight, C. 1967, Investigation of Sputtering Effects on the Moon's Surface Final Report, REPT.-3107, NASA, https://ntrs.nasa.gov/citations/19670028248
Wiens, R. C., Burnett, D. S., Calaway, W. F., et al. 1997, Icar, 128, 386
Wurz, P., & Lammer, H. 2003, Icar, 164, 1
Yakshinskiy, B. V., & Madey, T. E. 1999, Natur, 400, 642
Yakshinskiy, B. V., & Madey, T. E. 2003, SurSc, 528, 54
Yakshinskiy, B. V., & Madey, T. E. 2005, SurSc, 593, 202